Fibers and Polymers 2015, Vol.16, No.10, 2121-2129
DOI 10.1007/s12221-015-5429-0

ISSN 1229-9197 (print version)
ISSN 1875-0052 (electronic version)

Mesoporous $MgAl_2O_4$ and $MgTiO_3$ Nanoparticles Modified Polyacrylonitrile Nanofibres for 2-Chloroethyl Ethyl Sulfide Degradation

Arun Karthick Selvam and Gobi Nallathambi*

Department of Textile Technology, Anna University, Chennai 600025, India
(Received June 8, 2015; Revised September 2, 2015; Accepted September 3, 2015)

Abstract: Degradation of 2-chloroethyl ethyl sulfide (2-CEES), a stimulant of sulfur mustard, was investigated on the surface of polyacrylonitrile (PAN) nanofibres embedded with magnesium aluminate and magnesium titanate nanoparticles. The magnesium aluminate and magnesium titanate nanoparticles were prepared by the hydrothermal method and characterized by X-ray diffractometry, scanning electron microscopy and nitrogen adsorption BET. These metal oxide nanoparticles were mixed with PAN solution individually and then electrospun to produce nanofibres. Later, they were studied against the degradation of 2-CEES at room temperature (30±2 °C) using gas-chromatography coupled with flame ionization detector. The degradation and reaction kinetics data reveal that the 2-CEES degraded faster with higher amount of embedded metal oxide nanoparticles in PAN nanofibres. Moreover, the degradation yield of 2-CEES was higher in the case of PAN nanofibres embedded with magnesium aluminate nanoparticles relative to PAN nanofibres embedded with magnesium titanate nanoparticles. Fourier-transform infrared (FTIR) studies showed that the PAN nanofibres embedded with magnesium aluminate and magnesium titanate nanoparticles degrade 2-CEES by the formation of covalent/alkoxide bonds between the surface reactive oxide/hydroxyl group of metal oxide nanoparticles and 2-CEES. The result explores the role of modified PAN nanofibres with magnesium aluminate on the effective degradation of 2-CEES and possesses a suitable candidate for protective application.

Keywords: Magnesium aluminate, Magnesium titanate, 2-chloroethyl ethyl sulfide, Degradation, Electrospinning

Introduction

Chemical warfare agents (CWA) are one of the most mass destructive weapons created by the mankind [1]. All over the world, about 70 different chemicals or mixture of chemicals have been used or stockpiled as CWA for the purpose of military concern and terrorism [2]. CWA are classified in many ways. Based on their volatility, they are classified as persistent or non-persistent agents; and based on their chemical nature; they are classified as organophosphorus, organosulfur, organofluorine, and arsenicals. In common, by the physiological effects produced as a result of these agents on human beings, the CWA are classified as nerve agents, blister agents, blood agents, chocking agents, riot-control agents, and psychomimetic agents [3]. Among several CWA, mustard and nerve agents are well known for its higher toxicity and persistent nature [4,5]. Pure sulfur mustard (HD) is a colourless and odourless liquid while impure HD has the smell of mustard or garlic. Physiological effects of HD are serious skin burns and on inhalation affect the respiratory system, causing pulmonary edema. HD has the highest military significance since World War I owing to this agent irreversibly alkylates DNA, RNA, and protein, which leads to cell breakdown and death to incapacitate an enemy [6-8].

In earlier days, protective masks and protective garments filled with functionalised activated charcoal impregnated with Cu, Ag, Zn, and Mo worked by adsorption technique was used against the toxic chemicals that present as an aerosol or vapour in the battle field. The disadvantages of using these materials are heavy weight, moisture retention, and disposal of used masks and garments causes contamination by desorption [9,10]. At present, metal oxide nanoparticles, particularly MgO, TiO_2, CaO, Al_2O_3, Fe_2O_3 and zirconium based metal oxide shown enhanced chemical reactivity towards the breakup of HD to a nontoxic product at room temperature [11-16]. The process involved in effective decontamination of these deadly agents is hydrolysis, elimination, and oxidation reaction [17]. However, a suitable substrate is needed to mount these nanoparticles to use them as detoxifying agents in protective clothing and face masks [9,18,19].

Among various methods, electrospun nanofibers have the potential to incorporate reactive chemicals in it [10,20]. Characteristic features like high porosity, high surface area, high permeability, low basic weight, and small fibre diameter made eletrospun nanofibers a suitable protective agent against chemical and biological agents [10,18,21,22]. Gibson *et al.* and Schreuder-Gibson *et al.* studied that the thin layer electrospun membrane enhances the aerosol filtration with higher water vapour permeability [23-25]. Singh *et al.* reported self-decontaminating coating using organophosphorous hydrolase (OPH) enzyme that can breakdown organophosphorous pesticide rapidly [26]. By the same approach, Chen *et al.* and Han *et al.* prepared functionalised electrospun fibers with α-necleophilic moieties of oxime groups and tested against di-isopropyl fluorophosphates (DFP) [27,28]. Sundarrajan *et al.* found that the amount of paraoxon, a stimulant for nerve agent, was hydrolysed by polymer nanofibers containing MgO and TiO_2 nanoparticles [9,18].

Studies have shown that the polymeric nanofibers like

*Corresponding author: gobsnn@gmail.com

polyacrylonitrile (PAN) incorporated with metal oxide nanoparticles have the evidence of enhanced activation [29-31]. Oh *et al.* prepared PAN based activated carbon nanofibers embedded with manganese nanoparticles and studied against toluene adsorption. Their results showed that the higher specific area and bigger pore volume of nanoparticles increase the adsorption of toluene [30]. Recently, Beer Singh *et al.* reported the degradation of 2-chloroethyl ethyl sulfide (2-CEES) on the surface of vanadium oxide nanotubes and found the HD degrades faster relative to 2-CEES due to the porous structure and steric factor inside the pores of vanadium oxide nanotubes [32]. Due to the high toxic nature of HD, research studies were generally carried out with simulant 2-CEES. 2-CEES is one such simulant which has similar log K_{ow} value and the closest structure to HD [19,32,33]. Dadvar *et al.* investigated the decontamination ability of MgO and Al_2O_3 nanoparticles embedded activated PAN nanofibers. They found that decontamination yield of 2-CEES increases with increasing amounts of metal oxide nanoparticles in the nanofibers [19]. To the best of our knowledge, mixed metal oxide nanoparticles as single composite material have not been studied for the degradation of CWA. For the first time, magnesium aluminate and magnesium titanate nanoparticles embedded in PAN nanofibers was investigated for the decontamination and degradation kinetics study across 2-CEES in this report.

Experimental

Materials

Polyacrylonitrile (PAN) in powder form, a precursor, from Sigma-Aldrich India Ltd. and dimethylformamide (DMF), a solvent, from Merck India Ltd. were used to prepare electrospun PAN nanofibres incorporated with synthesised metal oxide nanoparticles of $MgAl_2O_4$ and $MgTiO_3$ nanoparticles. Magnesium nitrate hexahydrate, aluminium nitrate nonahydrate, butyl titanate, cetyl trimethyl ammonium bromide (C-TAB), and liquid ammonia of analytical grade from Merck India Ltd. are used to prepare metal oxide nanoparticles. 2-CEES of 98 % purity from Sigma-Aldrich India Ltd. and chloroform as solvent and decane as internal standard from SRL Chemicals India Ltd. were used in the degradation study of 2-CEES. All reagents were used as received.

Methods

Synthesis of Magnesium Aluminate Nanoparticles ($MgAl_2O_4$)

Magnesium aluminate nanoparticles were synthesised by hydrothermal method similar to Zhang *et al.* report [34]. Initially, stoichiometric amounts of magnesium nitrate and aluminum nitrate and desired amount of C-TAB were added in 50 m*l* distilled water. Under vigorous stirring, liquid ammonia was added drop by drop to adjust pH around 11. Then, the obtained material was heated at 180 °C for 24 h in a Teflon lined stainless steel autoclave. After completing hydrothermal treatment, the obtained solid product was washed with distilled water till the pH reaches 7, dried at 110 °C for 4 h, and then calcinated at 600 °C for 3 h.

Synthesis of Magnesium Titanate Nanoparticles ($MgTiO_3$)

The basic steps for the preparation of $MgTiO_3$ nanoparticles by hydrothermal method are described as follows:

(1) Ethanol solution containing magnesium nitrate and butyltitanate according to the mole ratio of Ti:Mg=1 was prepared.

(2) Desired amount of C-TAB was added and the rest is similar to the procedure of $MgAl_2O_4$ nanoparticles synthesis.

Preparation of Electrospun PAN Nanofibres Embedded with Metal Oxides

Solutions of 8 % PAN in DMF as solvent with three different wt. % of 10, 20, and 30 (w.r.t. polymer weight) containing magnesium aluminate and magnesium titanate nanoparticles were prepared. Metal oxide nanoparticles were added to DMF first and mixed under magnetic stirrer for 1 h to which 8 wt. % of PAN polymer was added and subsequently mixed by magnetic stirrer for 12 h at room temperature to form a homogenous solution. This was followed by ultra-sonication to achieve maximum dispersion of metal oxide nanoparticles in the prepared PAN solution. The prepared solution was then loaded in a 5 m*l* syringe fitted to a syringe pump. The positive terminal of a high voltage DC power supply with 15 kV of applied high voltage was connected to the 18 G metallic needle of the syringe. A grounded aluminium foil placed at 15 cm from the tip of the needle was used as the collector. The syringe pump was set to a feed rate of 0.5 m*l*/h. Formation of beads were observed when 6 wt. % of PAN solution and 8 wt. % of PAN solution with metal oxide greater than 30 wt. % were electrospun. The electrospinning process was carried out at room temperature with relative humidity of 45-50 %. The as-spun fibres were kept in vacuum for 24 h prior to further characterization.

Characterization

Powder X-ray diffraction (XRD) patterns were collected by Rigaku Rotaflex D/Max-C powder X-ray diffractometer with Cu Kα radiation (λ=0.154 nm) operated at 40 kV and 30 mA to identify the phase structure of the prepared metal oxide samples. Micrographs of the prepared PAN electrospun membrane were examined by scanning electron microscopy (SEM S3400 Hitachi) after gold sputter-coating using E 1010 Hitachi. Diameter of the electrospun fibres were measured manually using Image J software from the SEM image. The pore characteristics of the prepared metal oxide nanoparticles were determined from nitrogen isothermal adsorption-desorption characterization performance by Micromeritics ASAP 2020 adsorption meter at the liquid nitrogen temperature. The sample was degassed at 250 °C for 12 h before the measurement of data. The specific surface area was calculated

according to the BET method. The pore size distribution was calculated from the desorption branch of the isotherm by the Barrett, Joyner, and Halenda (BJH) method. Fourier-transform infrared (FTIR) spectra of the nanofibrous membrane were obtained from Bruker Tensor-27 FTIR spectrophotometer to identify the bond formation between embedded metal oxide nanoparticles and 2-CEES.

Reaction Procedure for 2-CEES Decontamination Studies

In order to study 2-CEES degradation ability, prepared PAN nanofibres embedded with $MgAl_2O_4$ and $MgTiO_3$ nanoparticles were made to react with 2-CEES. All reactions were performed in closed glass containers. A reaction solution containing a mixture of 20 m*l* chloroform and 10 μl of 2-CEES was prepared first and then mixed by shaker for 5 min. Before introducing the electrospun metal oxide embedded PAN nanofibre mat in to the reaction solution, 1 m*l* of the reaction solution was extracted as a control sample. Later, a 50 mg as-spun metal oxide nanoparticles embedded nanofibre mat was placed into the closed glass tube containing the reaction solution. The reaction was carried out at room temperature. After introducing the electrospun mat, about 1 m*l* of the reaction solution was extracted from the reaction glass container at time intervals of 5, 10, 20, 30, 60, 120, and 240 min and added to 1 μl of decane. To evaluate 2-CEES degradation, the extracted solutions were subjected to the gas chromatograph (GC) (Chemito 8610) equipped with BP5 column (60 m length and 0.25 mm internal diameter) and flame ionization detector. All GC analyses were performed in programming mode from 40 to 250 ^{o}C at a rate of 20 ^{o}C/min and held for 5 min to determine the remaining toxicants. The detector and injector port were maintained at 280 ^{o}C and 220 ^{o}C, respectively. The residual amount of 2-CEES was measured from the chromatogram of each sample in the end. The degradation percentage of 2-CEES was calculated by deducting residual amount from the initial amount of 2-CEES. In order to understand the degradation kinetics of 2-CEES on electrospun PAN metal oxide nanoparticle embedded nanofibrous mat, the values of kinetic rate constant of each samples were obtained by plotting a graph between log (a-x) versus time (t), where 'a' is the initial concentration of 2-CEES and 'x' is the degraded concentration of 2-CEES. Rate constant (k) values were calculated using the slope of the straight line drawn, and the values of half-life of reactions were calculated from 0.6932/k values. Since 2-CEES is highly toxic in nature, all the experiments were performed carefully using in the fume cupboard with applicable safety procedures.

Results and Discussion

Characterization of $MgAl_2O_4$ and $MgTiO_3$ Nanoparticles

Hydrothermal method was used to synthesis both $MgAl_2O_4$ and $MgTiO_3$ nanoparticles. These materials were characterized by X-ray diffraction technique in order to confirm the formation of $MgAl_2O_4$ and $MgTiO_3$ nanoparticles calcinated at 600 ^{o}C and the same is apparently shown in Figure 1. Figure 1(a) shows the powder XRD pattern of $MgAl_2O_4$ nanoparticles. The reflection peaks corresponding to Figure 1(a) at 18.9 ^{o}, 31.3 ^{o}, 36.6 ^{o}, 44.9 ^{o}, 59.5 ^{o}, 65.4 ^{o}, and 77.4 ^{o} 2θ which can be ascribed to the presence of (1 1 1), (2 2 0), (3 1 1), (4 0 0), (5 1 1), (4 4 0), and (5 3 3) diffraction peaks. These data reveal the formation of $MgAl_2O_4$ spinel-like phase and the same was consistent with previously reported data [35-37]. On the other hand, Figure 1(b) shows the XRD pattern of $MgTiO_3$ nanoparticles and the diffraction peaks at (0 0 3), (0 1 2), (1 0 4), (1 1 0), (1 1 3), (0 2 4), (1 1 6), (0 1 8), (2 1 4), (0 1 6), (2 1 4), (3 0 0), (2 0 8), (1 0 10), and (2 2 0) correspond to $MgTiO_3$ nanoparticles with minor phases of $MgTi_2O_5$ [38]. The average diameter of the particles calculated by Scherer's function using XRD profile is about 79.45 nm and 135.32 nm for $MgAl_2O_4$ and $MgTiO_3$, respectively.

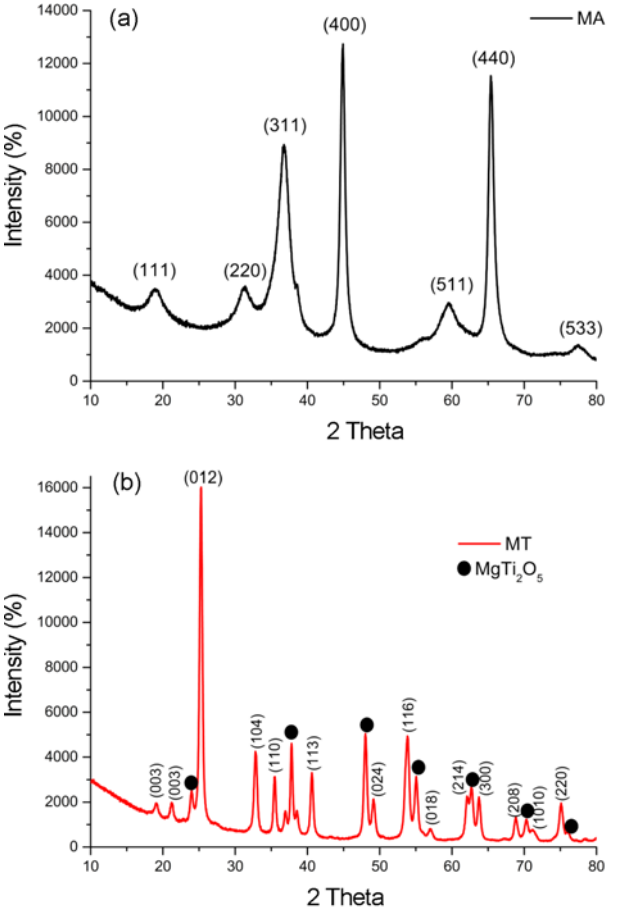

Figure 1. XRD pattern of (a) magnesium aluminate nanoparticles and (b) magnesium titanate nanoparticles.

The electron micrographs obtained by scanning electron microscopy of the prepared metal oxide nanoparticles were shown in Figure 2. Based on the SEM micrographs, the following remarks are pointed out in Figure 2. Figure 2(a)

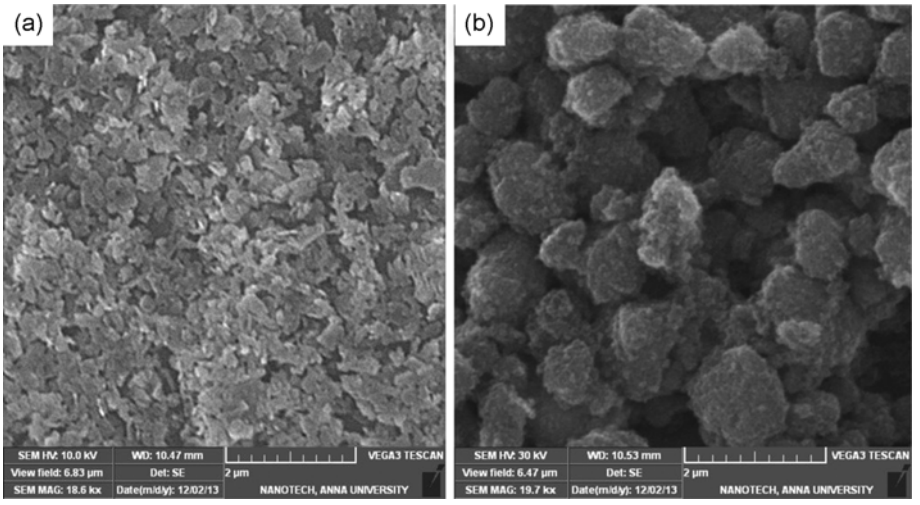

Figure 2. Scanning electron micrographs of metal oxide nanoparticles (a) magnesium aluminate nanoparticles and (b) magnesium titanate nanoparticles.

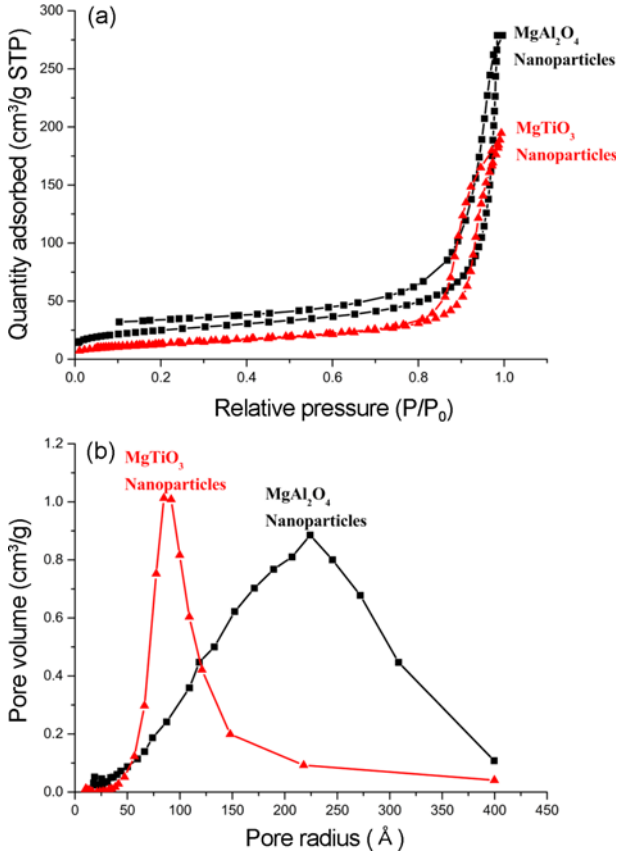

Figure 3. (a) N_2 adsorption/desorption isotherm and (b) pore size distribution of $MgAl_2O_4$ and $MgTiO_3$ nanoparticles.

and 2(b) show remarkable difference in grain size and morphologies as well as particle aggregation is large in Figure 2(b). The reason for the difference may be attributed by the heating process during hydrothermal treatment [39].

Figure 3(a) and 3(b) show the N_2 adsorption/desorption and pore size distribution of the prepared $MgAl_2O_4$ and $MgTiO_3$ nanoparticles. Figure 3(a) highlights that the N_2 adsorption capability of $MgAl_2O_4$ is higher compared with $MgTiO_3$ nanoparticles. In both metal oxide nanoparticles, it is seen that the sample showed mesoporous structure. According to IUPAC classification, the plateau shown by N_2 adsorption/desorption isotherm are of type III isotherm, with a H_3 type hysteresis loop. Table 1 shows the pore characteristics of $MgAl_2O_4$ and $MgTiO_3$ nanoparticles obtained from BET. As can be seen, $MgAl_2O_4$ nanoparticles show higher specific surface area, total pore volume, and average pore size comparative than $MgTiO_3$ nanoparticles.

Characterization of Nanofibres Membrane

Typical SEM image of PAN embedded with $MgAl_2O_4$ and $MgTiO_3$ nanoparticles in 10, 20, and 30 wt. % is shown in Figure 4. The average diameter of PAN metal oxide free nanofibre was about 500 nm (not shown here). In both case of adding $MgAl_2O_4$ and $MgTiO_3$ nanoparticles to PAN solution, the fibre diameter were reduced as observed from Table 2, which shows the average fibre diameter of PAN nanofibre embedded with $MgAl_2O_4$ and $MgTiO_3$ nanoparticles. This could be possibly due to the increase in conductivity by the addition of metal oxide nanoparticles in PAN solution.

Table 1. Pore characteristics of $MgAl_2O_4$ and $MgTiO_3$ nanoparticles

Sl. no.	Sample name	Specific surface area (m^2/g)	Total pore volume (cm^3/g)	Average pore radius (Å)
1.	$MgAl_2O_4$ nanoparticles	85.1115	0.4313	132.628
2.	$MgTiO_3$ nanoparticles	45.4979	0.3012	97.822

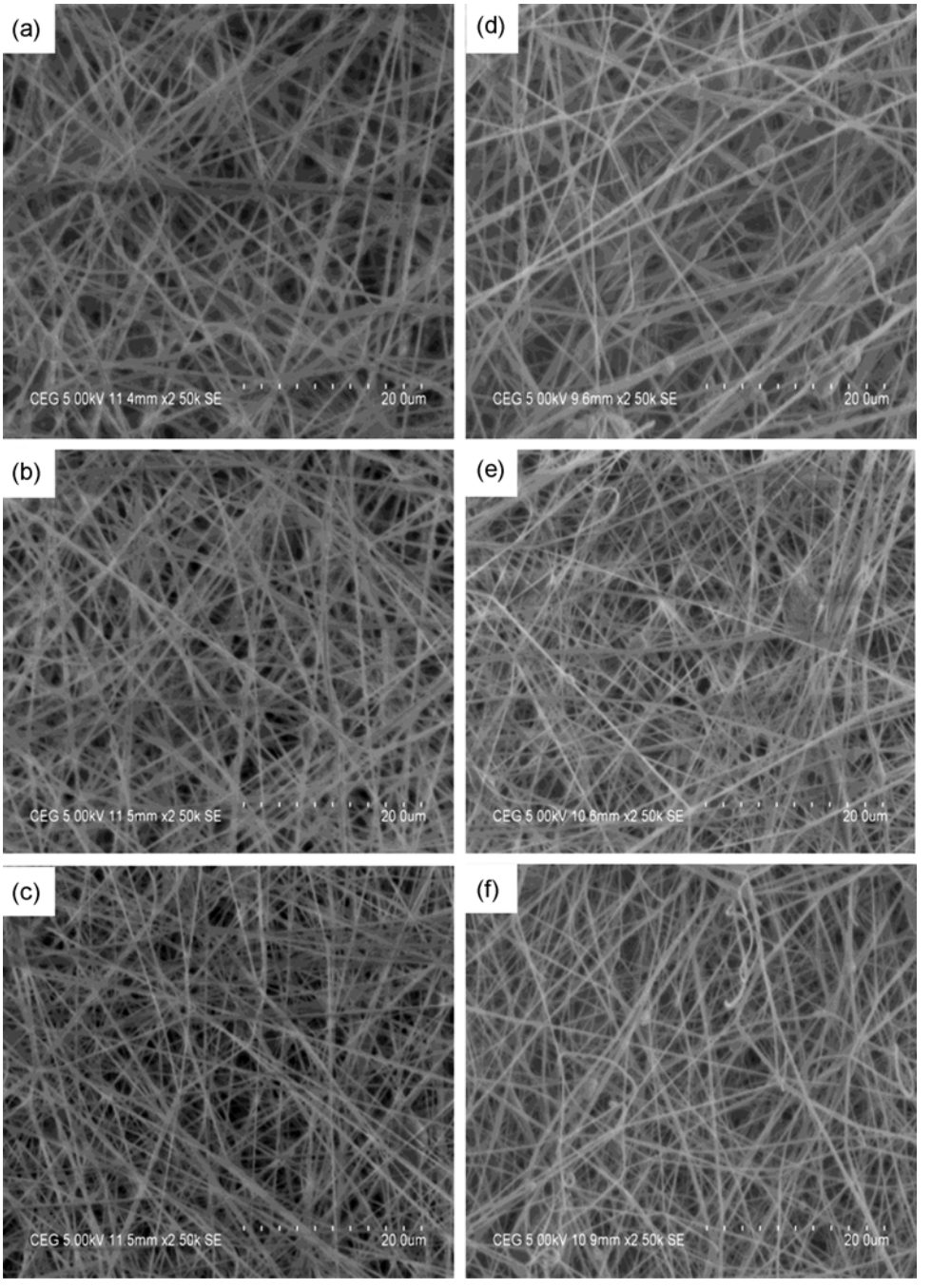

Figure 4. SEM image of PAN nanofibres embedded with $MgAl_2O_4$ and $MgTiO_3$ nanoparticles (a) PAN-MA-10, (b) PAN-MA-20, (c) PAN-MA-30, (d) PAN-MT-10, (e) PAN-MT-20, and (f) PAN-MT-30.

Table 2. Average fibre diameter of PAN nanofibre embedded with $MgAl_2O_4$ and $MgTiO_3$ nanoparticles

Sample name	Average fibre diametre (nm)	Sample name	Average fibre diametre (nm)	Sample name	Average fibre diametre (nm)
PAN nanofibres without nanoparticles	500	PAN-MA-10	282	PAN-MT-10	342
		PAN-MA-20	240	PAN-MT-20	281
		PAN-MA-30	214	PAN-MT-30	257

This result agrees with already reported literature [9,18]. By comparing the average fibre diameter, PAN nanofibre embedded with $MgAl_2O_4$ nanoparticles shows smaller fibre diameter than $MgTiO_3$ nanoparticles embedded PAN nanofibre. Interestingly, branched nanofibres are formed by the ejection of a secondary jet from the primary jet during electrospinning process [40]. Finally, the prepared samples by embedding metal oxide nanoparticles with 10, 20, and 30 wt. % were designated as PAN-MA-10, PAN-MA-20, and PAN-MA-30 for $MgAl_2O_4$ nanoparticles and PAN-MT-10, PAN-MT-20, and PAN-MT-30 for $MgTiO_3$ nanoparticles, respectively.

Degradation of 2-CEES

Figure 5 shows the degradation of 2-CEES for PAN nanofibres embedded with different wt. % of $MgAl_2O_4$ and $MgTiO_3$ nanoparticles. As can be seen, 2-CEES degradation occurs faster up to 60 min and then slows down, finally reaching an end at about 4 h. As can be seen from Figure 5, increase in metal oxide wt. % from 10 to 30 in PAN nanofibres shows increase in the degradation ability of 2-CEES. For PAN nanofibres with 10 wt. % of $MgAl_2O_4$ and $MgTiO_3$ nanoparticles show 2-CEES degradation of 57 % and 41 %, respectively. However, in case of PAN nanofibres with 30 wt. % of $MgAl_2O_4$ and $MgTiO_3$ nanoparticles showed increase in the 2-CEES degradation of 92 % and 73 %, compared with PAN nanofibres embedded with 20 and 10 wt. % of metal oxide nanoparticles, whereas polysulfone nanofibres incorporated with 35 wt. % of MgO showed only 75 % degradation [9]. A comparison on the degradation ability of the PAN nanofibres embedded with $MgAl_2O_4$ and $MgTiO_3$ nanoparticles shows a better degradation performance by PAN embedded with $MgAl_2O_4$ nanoparticles. The higher degradation yield of 2-CEES in case of PAN-MA-30 is related to the increase in the number of nanoparticles as well as the increase in the reactive sites as a result of bigger pore size of the embedded $MgAl_2O_4$ nanoparticles in PAN nanofibres.

Kinetic Degradation of 2-CEES

Figure 6(a) and 6(b) depict the kinetics of detoxification of 2-CEES on PAN-MA and PAN-MT nanofibres. The linear kinetic plot obtained between log (a-x) on Y-axis and time on X-axis exhibits that the initial part of 2-CEES degradation was faster followed by a steady state reaction confirmed the

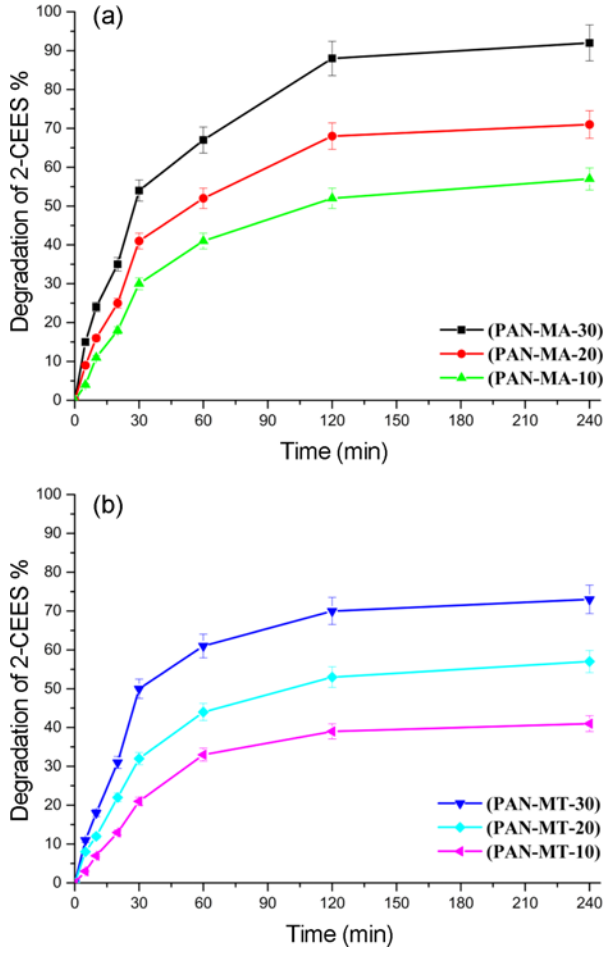

Figure 5. Degradation of 2-CEES for PAN nanofibres embedded with different wt. % of (a) $MgAl_2O_4$ and (b) $MgTiO_3$ nanoparticles.

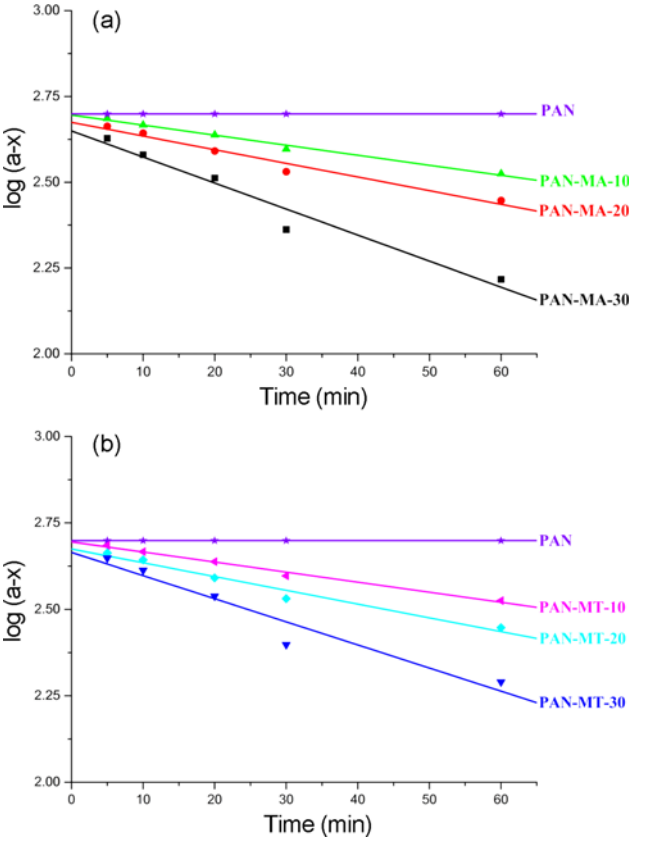

Figure 6. Kinetic degradation reaction of 2-CEES with (a) PAN-MA and (b) PAN-MT nanofibres.

Table 3. Kinetic data of the detoxification reaction of 2-CEES on PAN-MA and PAN-MT nanofibres

Sample name	Rate constant (min^{-1})	Half life (min)	Sample name	Rate constant (min^{-1})	Half life (min)
PAN-MA-10	0.0088	78.75	PAN-MT-10	0.0067	103.4328
PAN-MA-20	0.0118	58.73	PAN-MT-20	0.0092	75.32609
PAN-MA-30	0.0175	39.6	PAN-MT-30	0.0154	45

first order kinetics. The fast initial reaction is ascribed to the rapid adsorption and distribution of the 2-CEES within the pores and reacting with accessible reactive sites with PAN-metal oxide nanofibres. When the surface reactive sites are completely drained, the initial faster reaction was followed by steady state reaction. Basically, increasing the amount of $MgAl_2O_4$ and $MgTiO_3$ nanoparticles in the PAN nanofibres increases the reaction rate of the 2-CEES degradation (Figure 6). As a matter of fact, increasing the amount metal oxide nanoparticles from 10 wt. % to 30 wt. % in the PAN nanofibres roughly doubles the reaction rate. The reaction rate of PAN-MA nanofibres has superiority over PAN-MT nanofibres.

Table 3 shows the kinetic data of the detoxification reaction of 2-CEES on PAN-MA and PAN-MT nanofibres. The increase in the amount of metal oxide nanoparticles in PAN nanofibres leads to a generally higher number of nanoparticles, higher number of reactive sites of nanoparticles. The higher rate constant of PAN-MA in comparison with PAN-MT shows the role of the specific surface area, bigger pore size, and presence of more reactive sites in the detoxification process. This result agrees with the pervious results obtained by Li *et al.* and Lucas *et al.* that the higher surface area of metal oxide nanoparticles leads to higher number of surface reactive sites, which affects the chemical reactivity directly [41,42]. Table 3 shows all three wt. % PAN-MA nanofibres have a higher rate constant than PAN-MT nanofibres.

FTIR Spectra Analysis

Subsequently, we have characterized the samples by FTIR after drying it at room temperature for 24 h. Figure 7(a) and 7(b) show the IR spectra of PAN-MA-30 and PAN-MT-30 nanofibres before and after degradation of 2-CEES. The peak appearing at 1446 cm^{-1} in both PAN-MA-30 and PAN-MT-30 shows the formation of covalent/alkoxide bonds between the surface reactive oxide/hydroxyl groups of metaloxide nanoparticles and 2-CEES [43,44]. This investigation on the exposed samples revealed the destructive adsorption of 2-CEES by $MgAl_2O_4$ and $MgTiO_3$ nanoparticles embedded in PAN nanofibres. Martin *et al.* suggested that 2-CEES were bonded with the surface hydroxyl group of metal oxide by hydrogen bond [43]. Further, Narske *et al.* also suggested that the covalent bond formation will occur between surface oxide groups of metal oxides and methylene group of 2-CEES [44]. The typical FTIR transmittance at 690 and 540 cm^{-1} indicates the formation of surface complexes, showing the reaction between 2-CEES and metal oxide nanoparticles stops, however, the 2-CEES can reach the unreacted surface

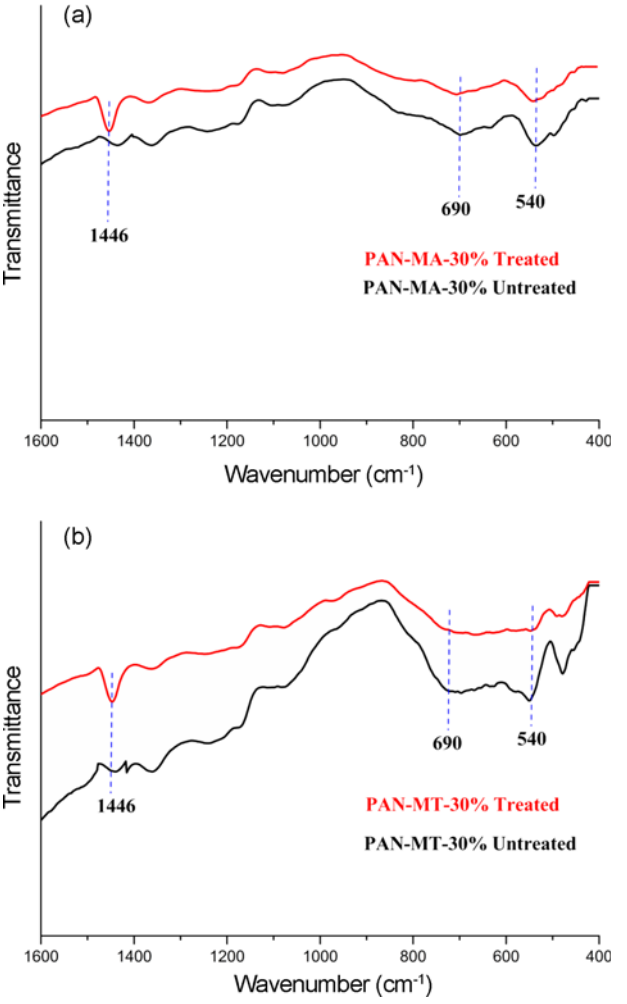

Figure 7. FTIR spectra of (a) PAN-MA-30 and (b) PAN-MT-30 nanofibres before and after treatment with 2-CEES.

by diffusion, thereby enhancing the reaction to reach a steady state in approximately 60 min. According to literature, the by-products formed by degradation of 2-CEES are held tightly inside the pores of the metal oxide nanoparticles; and as a result, they cannot pollute the environment upon disposal [13,14,45].

Conclusion

Magnesium aluminate and magnesium titanate nanoparticles were prepared by the hydrothermal method and characterized by XRD, SEM, and N_2 BET. PAN nanofibres with embedded

$MgAl_2O_4$ and $MgTiO_3$ nanoparticles were successfully made through electrospinning, and the degradation of 2-CEES were studied. The result showed that the prepared nanofibres with embedded metal oxide nanoparticles are promising reactive sorbent for the degradation and destruction of 2-CEES, and the study also shows that the degradation of 2-CEES depends on the pore size and number of reactive sites. Presence of bigger pore size and higher number of reactive sites in PAN-MA-30 sample gives the best degradation yield of 92 % against 2-CEES. The rate constant and half-life for PAN-MA-30 were found to be 0.0175 min^{-1} and 39.6 min, respectively. Fourier transform infrared studies showed that $MgAl_2O_4$ and $MgTiO_3$ nanoparticles embedded PAN nanofibres degrades and destroy 2-CEES by the formation of covalent/alkoxide bond between the reactive sites of $MgAl_2O_4$ and $MgTiO_3$ nanoparticles and 2-CEES.

Acknowledgments

The authors gratefully acknowledge the funding support from the Board of Research in Nuclear Sciences (BRNS), India under the project titled "Development of Nanocomposite Mask for NBC Application" under Sanction No. 2011/36/06-BRNS/156. The author Arun Karthick Selvam would also like to acknowledge University Grants Commission (UGC), India for providing him UGC-BSR fellowship.

Electronic Supplementary Material (ESM) The online version of this article (doi: 10.1007/s12221-015-5429-0) contains supplementary material, which is available to authorized users.

References

1. P. Aas, *Prehosp. Dis. Med.*, **18**, 306 (2003).
2. G. N. Volans and L. Karalliedde, *Lancet*, **360**, s35 (2002).
3. K. Ganesan, S. K. Raza, and R. Vijayaraghavan, *J. Pharm. Bioall. Sci.*, **2**, 166 (2010).
4. D. H. Ellison, "Handbook of Chemical and Biological Warfare Agents", 2nd ed., pp.131-143, CRC press, Baco Raton, New York, 2007.
5. L. Bromberg, H. Schreuder-Gibson, W. R. Creasy, D. J. McGarvey, R. A. Fry, and T. A. Hatton, *Ind. Eng. Chem. Res.*, **48**, 1650 (2009).
6. M. P. Shakarjian, D. E. Heck, J. P. Gray, P. J. Sinko, M. K. Gordon, R. P. Casillas, N. D. Heindel, D. R. Gerecke, D. L. Laskin, and J. D. Laskin, *Toxicol. Sci.*, **114**, 5 (2010).
7. A. Sharma, B. Singh, and A. Saxena, *Carbon*, **47**, 1911 (2009).
8. R. Singh, P. K. Gutch, and A. Mazumder, *Ind. Eng. Chem. Res.*, **52**, 4689 (2013).
9. S. Sundarrajan and S. Ramakrishna, *J. Mater. Sci.*, **42**, 8400 (2007).
10. R. Ramakrishnan, S. Sundarrajan, Y. Liu, R. S. Barhate, N. L. Lala, and S. Ramakrishna, *Nanotechnology*, **17**, 2947 (2006).
11. V. Štengl, M. Maříková, S. Bakardjieva, J. Šubrt, F. Opluštil, and M. Olšanská, *J. Chem. Technol. Biotechnol.*, **80**, 754 (2005).
12. G. W. Wagner, O. B. Koper, E. Lucas, S. Decker, and K. J. Klabunde, *J. Phys. Chem. B*, **104**, 5118 (2000).
13. G. W. Wagner, P. W. Batram, O. Koper, and K. J. Klabunde, *J. Phys. Chem. B*, **103**, 3225 (1999).
14. G. W. Wagner, L. R. Procell, R. J. O'Connor, S. Munavalli, C. L. Carnes, P. N. Kapoor, and K. J. Klabunde, *J. Am. Chem. Soc.*, **123**, 1636 (2001).
15. Neelam, V. Singh, and T. Gupta, *Anal. Chim. Acta,* **812**, 222 (2014).
16. S. Moon, Y. Liu, J. T. Hupp, and O. K. Farha, *Angew. Chem.*, **54**, 6795 (2015).
17. T. H. Mahato, G. K. Prasad, Beer Singh, A. R. Srivastava, K. Ganesan, J. Acharya, and R. Vijayaraghavan, *J. Hazard. Mater.*, **166**, 1545 (2009).
18. S. Sundarrajan, A. Venkatesan, and S. Ramakrishna, *Macromol. Rapid Commun.*, **30**, 1769 (2009).
19. S. Dadvar, H. Tavanai, M. Morshed, and M. Ghiaci, *J. Chem. Eng. Data*, **57**, 1456 (2012).
20. F. A. Sheikh, M. A. Kanjwal, S. Saran, W. J. Chung, and H. Kim, *Appl. Surf. Sci.*, **257**, 3020 (2011).
21. Y. C. Yang, J. A. Baker, and J. R. Ward, *Chem. Rev.*, **92**, 1729 (1992).
22. A. K. Selvam and G. Nallathambi, *Fiber. Polym.,* **16**, 1327 (2015).
23. P. Gibson, H. Schreuder-Gibson, and D. Rivin, *Colloid Surf. A-Physicochem. Eng. Asp.,* **187-188**, 469 (2001).
24. P. Gibson, H. Schreuder-Gibson, and D. Rivin, *AIChE. J.*, **45**, 190 (1999).
25. H. Schreuder-Gibson, P. Gibson, and Y. L. Hsieh, *Int. Nonwovens J.*, **11**, 21 (2002).
26. A. Singh, Y. Lee, and W. J. Dressick, *Adv. Mat.*, **16**, 2112 (2004).
27. L. Chen, L. Bromberg, H. Schreuder-Gibson, J. Walker, T. A. Hatton, and G. C. Rutledge, *J. Mater. Chem.*, **19**, 2432 (2009).
28. D. Han, S. Filocamo, R. Kirby, and A. J. Steckl, *ACS Appl. Mater. Interfaces*, **3**, 4633 (2011).
29. J. S. Im, S. J. Park, T. Kim, and Y. S. Lee, *Int. J. Hydrogen Energy*, **34**, 3382 (2009).
30. G. Y. Oh, Y. W. Ju, H. R. Jung, and W. J. Lee, *J. Anal. Appl. Pyrolysis*, **81**, 211 (2008).
31. C. Tekmen, Y. Tsunekawa, and H. Nakanishi, *J. Mater. Process. Technol*., **210**, 451 (2010).
32. B. Sing, T. H. Mahato, A. K. Srivastava, G. K. Prasad, K. Ganesan, R. Vijayaraghavan, and J. Rajeev, *J. Hazard. Mater*., **190**, 1053 (2011).
33. S. L. Bartelt-Hunt, D. R. U. Knappe, and M. A. Barlaz, *Crit. Rev. Environ. Sci. Technol.*, **38**, 112 (2008).
34. X. Zhang, *Mater. Chem. Phys.*, **116**, 415 (2009).

35. J. Guo, H. Lou, H. Zhao, X. Wang, and X. Zheng, *Mater. Lett.*, **58**, 1920 (2004).
36. C. Păcurariu, I. Lazău, Z. Ecsedi, R. Lazău, P. Barvinschi, and G. Mărginean, *J. Eur. Ceram. Soc.*, **27**, 707 (2007).
37. E. N. Alvar, M. Rezaei, and H. N. Alvar, *Powder Technol.*, **198**, 275 (2010).
38. Y. M. Miao, Q. L. Zhang, H. Yang, and H. P. Wang, *Mater. Sci. Eng. B*, **128**, 103 (2006).
39. A. Troia, M. Pavese, and F. Geobaldo, *Ultrason. Sonochem.*, **16**, 136 (2009).
40. A. Greiner and J. H. Wendorff, *Angew. Chem. Int. Ed.*, **46**, 5670 (2007).
41. Y. X. Li, O. Koper, M. Atteya, and K. J. Klabunde, *Chem. Mater.*, **4**, 323 (1992).
42. E. Lucas, S. Decker, A. Khaleel, A. Seitz, S. Fultz, A. Ponce, W. Li, C. Carnes, and K. J. Klabunde, *Chem. Eur. J.*, **7**, 2505 (2001).
43. M. E. Martin, R. M. Narske, and K. J. Klabunde, *Microporous Mesoporous Mat.*, **83**, 47 (2005).
44. R. M. Narske, K. J. Klabunde, and S. Fultz, *Langmuir*, **18**, 4819 (2002).
45. O. B. Koper, S. Rajagopalan, S. Winecki, and K. J. Klabunde in "Environmental Applications of Nanomaterials", 2nd ed. (G. E. Fryxell and G. Cao Eds.), pp.3-24, Imperial College Press, London, 2007.